Supplemental Material for

A VDAC1-mediated NEET protein chain transfers [2Fe-2S] clusters between the mitochondria and the cytosol and impacts mitochondrial dynamics

Ola Karmi[a,b*], Henri-Baptiste Marjult[a*], Fang Bai[c,d,e,f], Susmita Roy[g], Yang-Sung Sohn[a], Merav Darash Yahana[a], Faruk Morcos[h], Konstantinos Ioannidis[a,i], Yaakov Nahmias[a,i], Patricia A. Jennings[j], Ron Mittler[b], Jose' N. Onuchic[c,d,e**] and Rachel Nechushtai[a**]

[a] The Alexander Silberman Institute of Life Science and The Wolfson Centre for Applied Structural Biology, Faculty of Science and Mathematics, The Edmond J. Safra Campus at Givat Ram, The Hebrew University of Jerusalem, Jerusalem, 91904, Israel.
[b] Department of Surgery, University of Missouri School of Medicine, Christopher S. Bond Life Sciences Center, University of Missouri, 1201 Rollins St, Columbia, MO 65211, USA.
[c] Center for Theoretical Biological Physics, Department of Physics and Astronomy, Rice University, Houston, TX 77005.
[d] Department of Chemistry, Rice University, Houston, TX 77005.
[e] Department of Biosciences, Rice University, Houston, TX 77005.
[F] Shanghai Institute for Advanced Immunochemical Studies and School of Life Science and Technology, ShanghaiTech University, Shanghai, China, 201210.
[g] Indian Institute of Science Education and Research (IISER)- Kolkata, Campus Road, Mohanpur, West Bengal 741246, India.
[h] Departments of Biological Sciences and Bioengineering, University of Texas at Dallas, Richardson, TX 75080.
[I] Alexander Grass Center for Bioengineering, The Hebrew University of Jerusalem, Edmond J. Safra Campus at Givat Ram, Jerusalem 91904, Israel.
[j] Department of Chemistry & Biochemistry, University of California at San Diego, La Jolla, CA 92093.

[*]Equally contributed to the experimental work presented

[**]To whom correspondence should be addressed: Rachel@mail.huji.ac.il or Jonuchic@rice.edu

Supplemental Information:

MiNT protein expression affects the cellular ROS formation

MiNT protein was down regulated by 50% or over expressed by 10X in MDA-MB-231 cells (Figure supplemental 1 A.), this was not affecting the expression of VDAC1 protein (Figure S6), but it affected the mNT expression by over-expressing the mNT in both cell lines (Figure 1 A.). The effect of the MiNT protein overexpressed was important that it increased the cells resistance to mROS formation upon stimulating the ROS using H_2O_2, as shown in (Figure Supplemental 1 B.). All the effects described in these cells were connected to the accumulation of the mitochondrial labile iron (mLI) in both forms of MiNT expression (Figure Supplemental 1 C.). The high increase of mLI was also activating the overaccumulation of mROS (Figure Supplemental 1 D.), as well as destroying the mitochondrial membrane potential (MMP) (Figure Supplemental 1 E.). All of the previous mentioned mLI, mROS overaccumulation and MMP deformation was able to be corrected upon treating the cells with the mild iron chelator Deferiprone (DFP), in which restored all of these parameters back to be normal (Figure Supplemental 1 C.-E.).

Changing the cellular MiNT expression affecting the mitochondrial morphology and structure

Transmission electron microscope (TEM) investigation for the MDA-MB-231 cells with the different expression levels of the inner mitochondrial MiNT protein; showed high morphological abnormalities in the mitochondria in the lines of MiNT(-) and MiNT(+) compared to the normal levels in the control cells (Figure Supplemental 2 A+B). Abnormal mitochondrial morphology included the inner crista structure and the outer mitochondrial membrane.

Mitochondrial function and glycolysis activity were changed in the different MiNT expressing cell lines

Decreasing the expression of MiNT(-) cells was connected to fission feature of the mitochondria, but it showed high oxygen consumption rate (OCR) parameters in these cells compared to control (Figure Supplemental 3 A.), the increased OCR activity was connected to increased respiration and ATP production ability. On the other hand, increasing the expression of the MiNT(+) protein that was connected to high fusion of the mitochondria, was almost similar to slight decrease the activity of the OCR parameters compared to control cells (Figure Supplemental 3. A.). Bothe changes in the MiNT expression levels MiNT(-) or MiNT(+) were able to increase the glycolysis activity in the cells compared to control cells (Figure Supplemental 3 B.).

Binding Site Identification Method

To identify potential binding sites for a protein, we designed a molecular probe library, which includes small organic molecules and peptide elements, i.e., side chains of residues. Organic molecules can be used to search for the ‘druggable sites’, and peptide probes can be used to determine the potential protein-protein interface. In this work, we only chose peptide probes to search on the surface of MiNT and mNT separately by using the molecular docking tool iFitDock [53]. The cut off set as the filtering criteria to select the candidate binding modes of the molecular probes was set as 0.0kcal/mol. In other word, if the calculated binding affinity for the predicted binding mode is lower than 0, it will be kept and sent to the next clustering stage because we

thought it may bind with the protein, though their binding affinity is relatively weak. Then DBSCAN algorithm is designed to cluster the observed binding modes of all probes on the protein surface. In the first step, the binding modes for each probe type are clustered with a cluster member neighborhood radius of 3.0 Å and a minimum cluster density of 5. The center point of each binding mode cluster and the binding mode with the lowest binding affinity in each cluster are collected as the input for the second step clustering process. If the center point of a binding mode is the one with the lowest binding affinity in one cluster, only the center point of the binding mode is kept. In the second step, the collected binding modes for all the probes in the previous step are clustered with a cluster member neighborhood radius of 4.0 Å and a minimum cluster density of 10. Finally, three candidate binding sites for each protein were identified, as illustrated in Figure S4. The Site 1 and Site 2 of mNT can be approximated as the same site, which two sites have a large portion of overlap on the compositions of residues from the different chains.

Computational Modeling of Binding Poses

To understand how these three proteins interact with each other, a computational prediction and modeling framework was designed to predict the ternary complex and characterize their recognition process. First, as described in the above section, we used our in-house protein-protein interaction (PPI) binding site identification method Fd-DCA [41] to search potential sites on the surface of the soluble domain of mNT (homodimer) (PDB code: 2QH7) and MiNT(PDB code: 6AVJ). As a result, we identified three candidate binding sites for each of them, as shown in Figure S4. The potential Site 1 and Site 2 of mNT are almost symmetric, having a substantial number of overlapped residues. The residue composition of each site is described at the bottom of Figure S4. Then we used HADDOCK [43], a protein-protein docking webserver, to predict the binding pose for mNT-MiNT. To determine which two binding sites interact, we performed this calculation for each pair of proteins. For every candidate site of mNT or MiNT, we chose two residues located around the center position as the active residues required as the constraints for the docking simulations. Interestingly, despite using different combinations of candidate sites for each pair of proteins, similar binding poses for each protein complex were obtained, showing little variance of orientations or conformation. With the aid of the investigation of visual inspection, the largest cluster among these results was kept as the potential binding pose of mNT-MiNT. The cluster has a size of 400 binding poses was selected, which has a HADDOCK score of -106.4$\pm$9.3, and the RMSD from the overall lowest-energy structure is 1.3$\pm$0.8. For VDAC1, we can not accurately specify the active sites or residues. Theoretically, any protein which interacts with VDAC1, should insert into the large tunnel, forming a circular set of contacts with the inner residues of VDAC1. But it is important to point out that we needed to pick serveral residues located inside of the tunnel (uniformly distributing through the tunnel) to search the binding poses of CISD1 or CISD3 inside of the tunnel but not outside. The experimental structure of VDAC1 with the PDB code of 3EMN was used for constructing a ternary complex with the modeled dimer of mNT-MiNT. The tunnel of the experimentally determined *apo* structure of VDAC1 is not large enough to accommodate the predicted binding complex of mNT-MiNT. Therefore, to construct the ternary complex of mNT-MiNT-VDAC1, all the predicted binding poses of mNM-VDAC1, MiNT-VDAC1 as well as mMT-MiNT were fully considered, those binary conformations were artificially adjusted to form a reasonable ternary complex; therefore, the binding scores for the original binary complexes were

not provided. Then, the constructed primary ternary complex was conformationally refined by using the steepest descent energy minimization method with implicit solvent. The initial model was subject to OPLS all-atom force field [60] and the set of parameters available in GROMACS package. To calculate the electrostatic interactions, we used particle-mesh Ewald (PME) [61] with a grid spacing of 0.12 nm and an interpolation order of 4. The constructed ternary binding complex is shown in Figure 3D. mNT binds with VDAC1 mainly via its Site 2 and part of the Site1 and uses its large area of Site 1 to interact with the Site1 of MiNT. Besides, Site 2 and Site 3 of MiNT are the major areas that contribute to the contacts with VDAC. Finally, we used a coarse-grained molecular dynamic simulation to describe the recognition process between mNT and MiNT via the VDAC1, (see movie S1 in the SI). This analysis revealed that the relatively smaller protein MiNT can quickly tunnel into one side of VDAC1 and form a stabilized binary complex. mNT takes a bit longer to find a suitable orientation to insert itself into the VDAC1 from the other side of VDAC1 until it forms a well-packed ternary complex.

Coarse-grained Structure-based Simulations

To understand the dynamic binding mechanism of the above ternary complex, a structure-based coarse-grained simulation approach has been adopted. The residue-residue interacting contacts obtained from the pair-wise docking simulations described in the previous section can be utilized to construct a structure-based Hamiltonian for the formation of the trimeric assembly VDAC1-mNT-MiNT. The complete Hamiltonian is comprised of two terms: $V_{\text{intra}}, V_{\text{inter}}$. The complete Hamiltonian as a function of a set of position coordinates $\left\{\vec{r}_i\right\}$ has the following simple form:

$$V\left\{\vec{r}_i\right\} = V_{\text{intra}} + V_{\text{inter}} \qquad \text{(Eqn. S1)}$$

where, V_{intra} describes intra-chain interactions/contacts for VDAC, mNT and MiNT to maintain their internal local and non-local interactions.

$$V_{intra} = V_{intra}^{VDAC1} + V_{intra}^{mNT} + V_{intra}^{MinT} \qquad \text{(Eqn. S2)}$$

The local part of $V_{\text{intra}}^{\text{VDAC1/mNT/MiNT}}$ includes harmonic potentials that restrain bonds (r) and angles (θ). Dihedral angles (ϕ) are treated with a cosine term, as shown in Eqn. S4. The initial geometric parameters $(r_i^0,\ \theta_i^0, \phi_i^0, r_{ij}^0)$ are obtained from their individual PDB structures.

$$V_{\text{intra}}^{\text{VDAC1/mNT/MiNT}} = \underbrace{\sum_{i}^{bonds} \frac{\varepsilon_r}{2}\left(r_i - r_i^0\right)^2 + \sum_{i}^{angles} \frac{\varepsilon_\theta}{2}\left(\theta_i - \theta_i^0\right)^2 + \sum_{i}^{dihedral} \varepsilon_\phi^{(n)} F_D\left(\phi_i - \phi_i^0\right)}_{\text{Local}}$$

$$+ \underbrace{\sum_{i<j-3} \varepsilon_c \left(5\left(\frac{r_{ij}^0}{r_{ij}}\right)^{12} - 6\left(\frac{r_{ij}^0}{r_{ij}}\right)^{10} \right) \Delta_{\text{ij}} + \sum_{i<j-3}^{\text{intra-non-contacts}} \varepsilon_{NC} \left(\frac{\sigma}{r_{ij}}\right)^{12} \left(1\text{-}\Delta_{\text{ij}}\right)}_{\text{Non-local}}$$

(Eqn. S3)

Where, $F_D(\phi) = \left[1-\cos(\phi)\right] + \frac{1}{2}\left[1-\cos(3\phi)\right]$ (Eqn. S4)

The first non-local term of the Hamiltonian used in $V_{\text{intra}}^{\text{VDAC1/mNT/MiNT}}$ represents the non-bonded interaction potential in the form of 10–12 Lennard-Jones potential that is used to describe the interactions that stabilize the interacting contacts found from docking simulations [54]. For a pair of residue positions (*i* and *j*), a contact is defined when (*i*–*j*)>3. To avoid energetic over-counting shadow criteria were used in contact-pair counting [55]. Δ_{ij} is defined in such a way that if any *i* and *j* residues belong to $V_{\text{intra}}^{\text{VDAC1/mNT/MiNT}}$, Δ_{ij} = 1 turning on 10–12 Lennard-Jones potential; otherwise Δ_{ij} = 0. For all non-native pairs for which Δ_{ij} = 0, a repulsive potential with σ = 4Å is used.

The second term in (Eqn. S1), V_{inter} includes only non-local inter-chain PPI contact pairs for VDAC1-mNT, mNT-MiNT, as well as for VDAC1-MiNT. Therefore, V_{inter} accounts for all the dimeric interfaces as expressed below:

$$V_{inter} = V_{inter}^{\text{VDAC1-mNT}} + V_{inter}^{\text{mNT-MiNT}} + V_{inter}^{\text{VDAC1-MiNT}} \quad \text{(Eqn. S5)}$$

$$V_{inter}^{\text{VDAC1-mNT/mNT-MiNT/VDAC1-MiNT}} = \sum_{ij} \varepsilon_c \left(5\left(\frac{r_{ij}^0}{r_{ij}}\right)^{12} - 6\left(\frac{r_{ij}^0}{r_{ij}}\right)^{10} \right) \Delta_{\text{ij}} + \sum_{i} \varepsilon_{NC} \left(\frac{\sigma}{r_{ij}}\right) \left(1-\Delta_{\text{ij}}\right) \quad \text{(Eqn. S6)}$$

Similar to our previous approach [56], Δ_{ij} =1 if any *i* and *j* residues belong to any dimeric interfacial contact-pair list, turning on 10–12 Lennard-Jones potential; otherwise Δ_{ij} = 0.

Stochastic Simulations

Every kinetic simulation has begun from individual and energetically minimized structures of VDAC, mNT, and MiNT. These three separated components are kept in a large cubic box of 100 nm length, maintaining equal moderate proximity between each pair. Atomic coordinates of these energy minimized structures have been evolved using Langevin dynamics with a time step of $0.0005\ \tau_R$ using the structure-based Hamiltonian constructed above (Eqn. S1). We used an underdamped condition for rapid sampling [57]. For explicit particles, reduced mass $1\ \mu_R$ and a drag coefficient $1\ \tau_R^{-1}$ are used to sample the conformational space [54, 58] efficiently, where $\tau_R = \left(\frac{m\sigma^2}{\varepsilon_c}\right)^{0.5}$. To observe the ternary complex formation, coarse-grained kinetic simulations were performed albeit at a lower reduced temperature ($T^*=0.48T_R$). Standard structure-based

models implemented in Gromacs (SMOG) were used for all the simulations [59]. We have used the same parameter set as the one in structure-based coarse-grained simulations in our earlier studies [56] .

Supplemental Figure Legends:

Figure S1: MiNT protein expression affects the cellular ROS formation that is related to iron accumulation in the mitochondria. A. Western blot analysis against MiNT antibody normalized to β-actin for the Control, MiNT(-) and MiNT(+) lines showing the downregulation of MiNT(-) line (red dots) compared to control (black dots) (left) and the overexpression of MiNT(+) (gray dots) compared to control (black dots) (right). Results are presented as box and whiskers plots and include all data points measured in three different experiments. ****P <0.001*; Student's T-test, from three different experiments. B. Confocal fluorescence microscope images (left) for cellular ROS in MiNT(+) *vs.* control upon stimulating ROS generation with H_2O_2 (50μM), showing ROS resistance in the MiNT(+) lines over time. (Right) analysis for the ROS formation over 60 minutes in the MiNT(+) (gray line) compared to control cells (black line) upon H_2O_2 administration. Results expressed as mean ± SD for all time points, from three different experiments. C. Graph representing RPA fluorescence for all cell lines (Control, MiNT(-) and MiNT(+)) showing increased accumulation of mLI (quenching of RPA fluorescence) (white boxes), and the RPA change after using DFP to treat the cells (gray boxes), showing increase in the RPA fluorescence (correction). Results are presented as box and whiskers plots and include all data points measured in three different experiments. ****P <0.001*; Student's T-test, from three different experiments. D. Graph representing mito-SOX™ fluorescence for all cell lines (Control, MiNT(-) and MiNT(+)) showing increased mROS formation over time (white boxes), and the mROS correction after using DFP to treat the cells (gray boxes). Results are presented as box and whiskers plots and include all data points measured in three different experiments. ****P <0.001*; Student's T-test, from three different experiments. E. Graph representing TMRE fluorescence for all cell lines (Control, MiNT(-) and MiNT(+)) showing disrupting the MMP with decreased fluorescence (white boxes), and the correction of the MMP after using DFP to treat the cells (gray boxes). Results are presented as box and whiskers plots and include all data points measured in three different experiments. ****P <0.001*; Student's T-test, from three different experiments.

Figure S2: MiNT expression changing in cells affecting the mitochondrial morphology and structure. A. TEM images of the MDA-MB-231 different cell lines of Control, MiNT(-) and MiNT(+) showing the mitochondrial structure and morphology. B. Graph showing the analysis of the abnormal mitochondrial structure in the Control cells (black dots), MiNT(-) line (red dots) and MiNT(+) line (gray dots). Results are presented as mean ± SD from three different experiments. ****P <0.001*; Student's t-test.

Figure S3: Seahorse measurements for oxygen consumption rate (OCR) and Extracellular acidification rate (ECAR) for the different MiNT expressing lines. A. (Upper) Seahorse-generated plots of mitochondrial respiration obtained for the different lines. Data is presented in normalized values. (Lower) different parameters calculated from the upper panel, summarizes the different mitochondria related activities. B. (Upper) Seahorse-generated plots of ECAR obtained for the different lines. Data is presented in normalized values. (Lower) different parameters

calculated from the upper panel, summarizes the different glycolysis parameters in the cells. Results in (A and B) were normalized to the number of cells used (25,000). Data in the lower panels are presented as columns expressing mean ± SD and include all data points measured in three different experiments. **P<0.05, **P<0.01, ***P<0.001*; Student's t-test, N=3.

Figure S4: The potential sites on the surface of the soluble domain of mNT (homodimer) and MiNT, showing the three candidate binding sites for each of them. A. (Upper) Three candidate binding sites for mNT, named as Site 1, Site 2 as well as Site 3, and highlighted in different color. The residues covered in each site has listed below each subfigure. B. The lower shows the site identification results for MiNT.

Figure S5 (Movie S1): The movie shows a dynamic recognition process among the MiNT, VDAC1 and mNT. They were colored in light purple, orange, and light green, respectively. This is a coarse-grained model, hence the [2FE-2S] clusters were not included.

Figure S6: VDAC1 protein expression upon variable MiNT expression in MDA-MB-231 Breast cancer cells. Western blot analysis using VDAC1 antibody normalized to β-actin for Control, MiNT(-) and MiNT(+) lines. Results are presented as box and whiskers plots and include all data points measured in three different experiments.

Table S1: Identification of proteins that interact with MiNT following Co-IP with an anti MiNT antibody applied to an enriched mitochondrial fraction from MDA-MB-231 cells. The cut-off of abundance was determined by the abundance of MiNT protein in the sample.

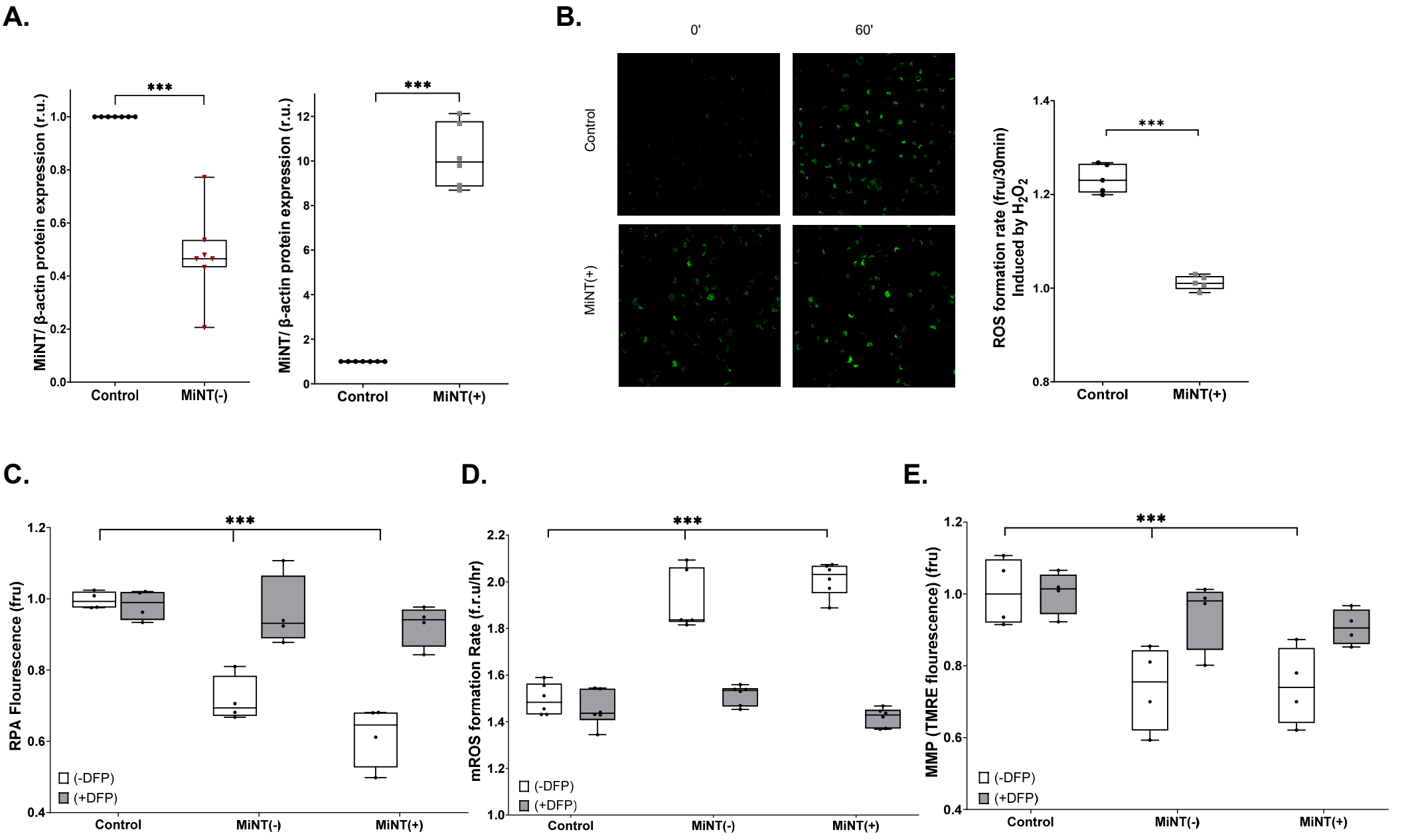
A.
***
MiNT/ β-actin protein expression (r.u.)
1.0
0.8
0.6
0.4
0.2
0.0
Control
MiNT(-)
***
MiNT/ β-actin protein expression (r.u.)
12
10
8
6
4
2
0
Control
MiNT(+)
B.
0'
60'
Control
MiNT(+)
***
ROS formation rate (fru/30min)
Induced by H2O2
1.4
1.2
1.0
0.8
Control
MiNT(+)
C.
***
RPA Flourescence (fru)
1.2
1.0
0.8
0.6
0.4
(-DFP)
(+DFP)
Control
MiNT(-)
MiNT(+)
D.
***
mROS formation Rate (f.r.u/hr)
2.2
2.0
1.8
1.6
1.4
1.2
1.0
(-DFP)
(+DFP)
Control
MiNT(-)
MiNT(+)
E.
***
MMP (TMRE flourescence) (fru)
1.2
1.0
0.8
0.6
0.4
(-DFP)
(+DFP)
Control
MiNT(-)
MiNT(+)

Figure S1

A.

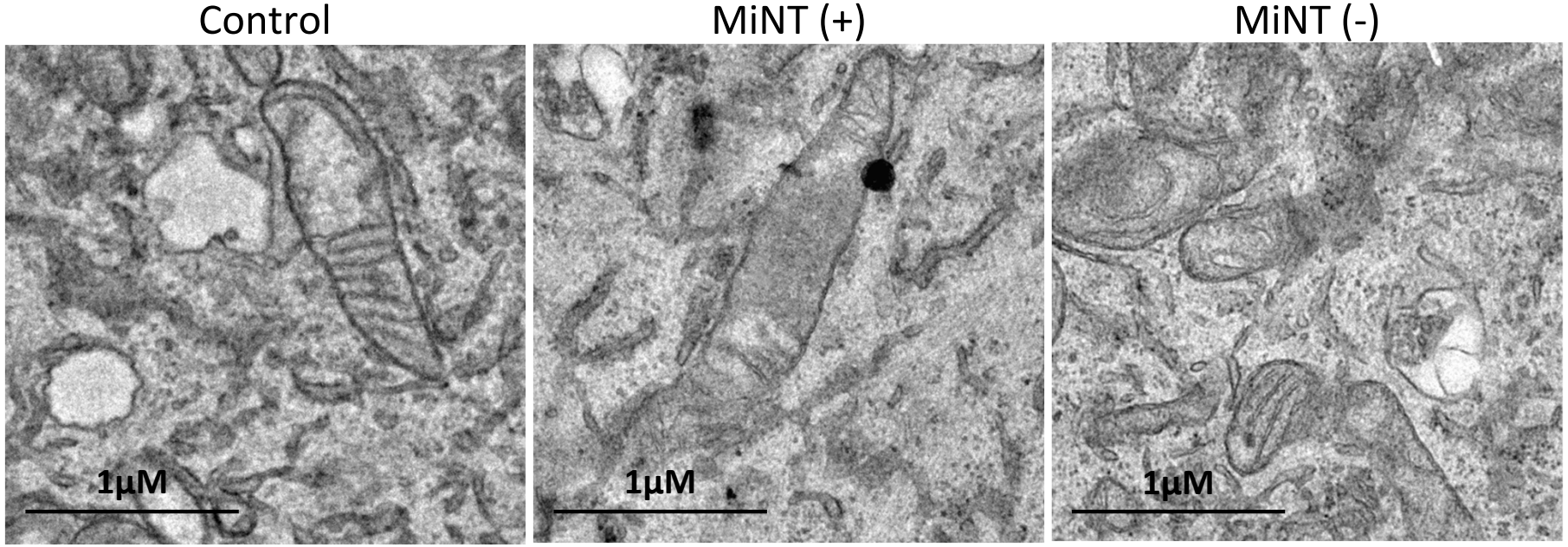
Control
MiNT (+)
MiNT (-)
1μM
1μM
1μM

B.

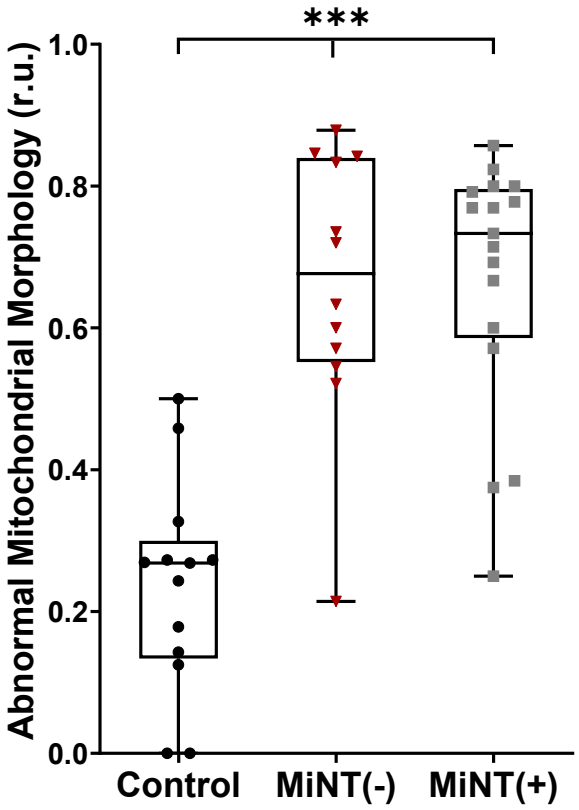
***
Abnormal Mitochondrial Morphology (r.u.)
1.0
0.8
0.6
0.4
0.2
0.0
Control
MiNT(-)
MiNT(+)

Figure S2

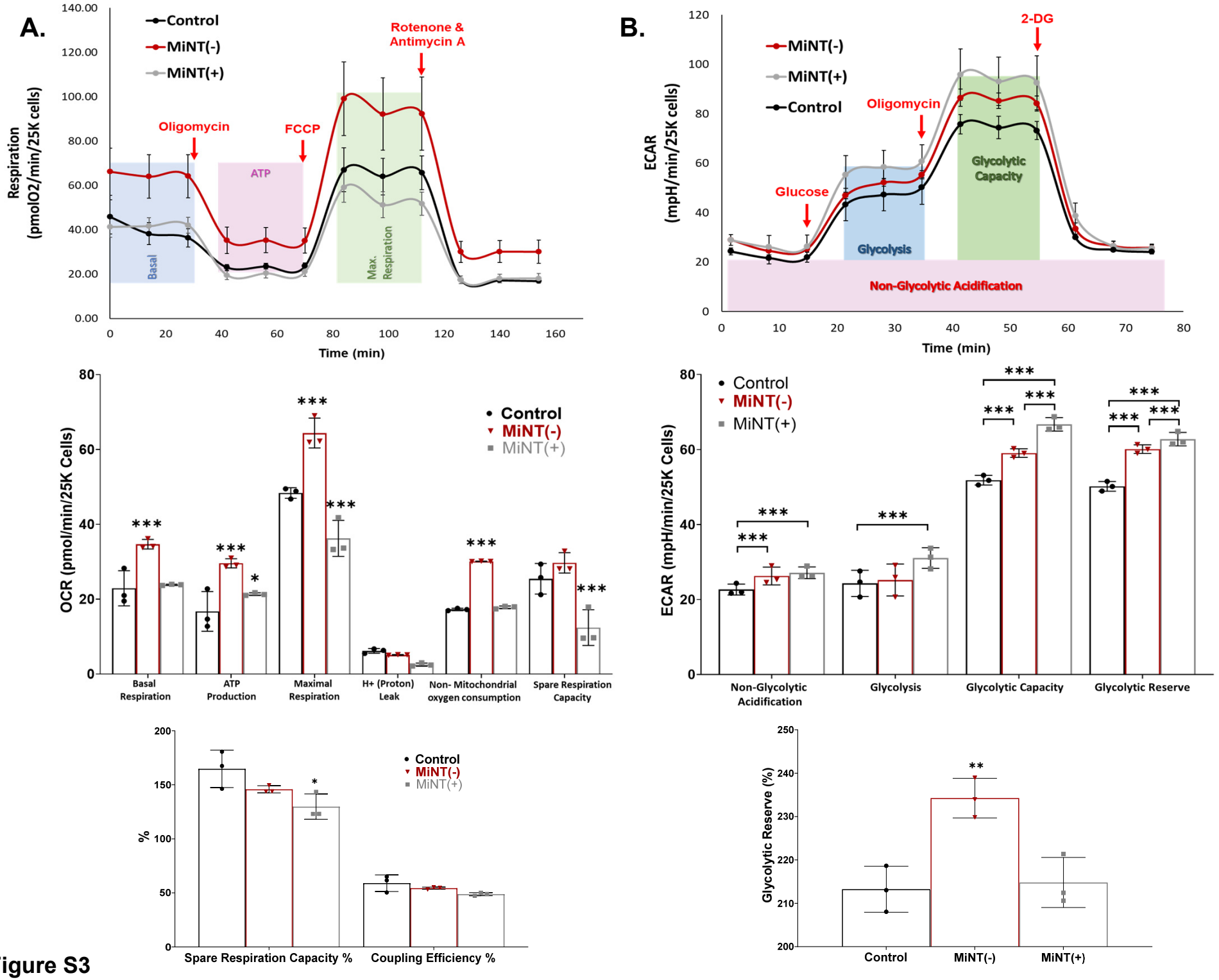
A.
Control
MiNT(-)
MiNT(+)
Rotenone &
Antimycin A
Oligomycin
FCCP
ATP
Basal
Max.
Respiration
Respiration
(pmolO2/min/25K cells)
Time (min)
B.
MiNT(-)
MiNT(+)
Control
2-DG
Oligomycin
Glycolytic
Capacity
Glucose
Glycolysis
Non-Glycolytic Acidification
ECAR
(mpH/min/25K cells)
Time (min)
Control
MiNT(-)
MiNT(+)
OCR (pmol/min/25K Cells)
Basal
Respiration
ATP
Production
Maximal
Respiration
H+ (Proton)
Leak
Non- Mitochondrial
oxygen consumption
Spare Respiration
Capacity
ECAR (mpH/min/25K Cells)
Non-Glycolytic
Acidification
Glycolysis
Glycolytic Capacity
Glycolytic Reserve
%
Spare Respiration Capacity %
Coupling Efficiency %
Glycolytic Reserve (%)
Control
MiNT(-)
MiNT(+)

Figure S3

A.

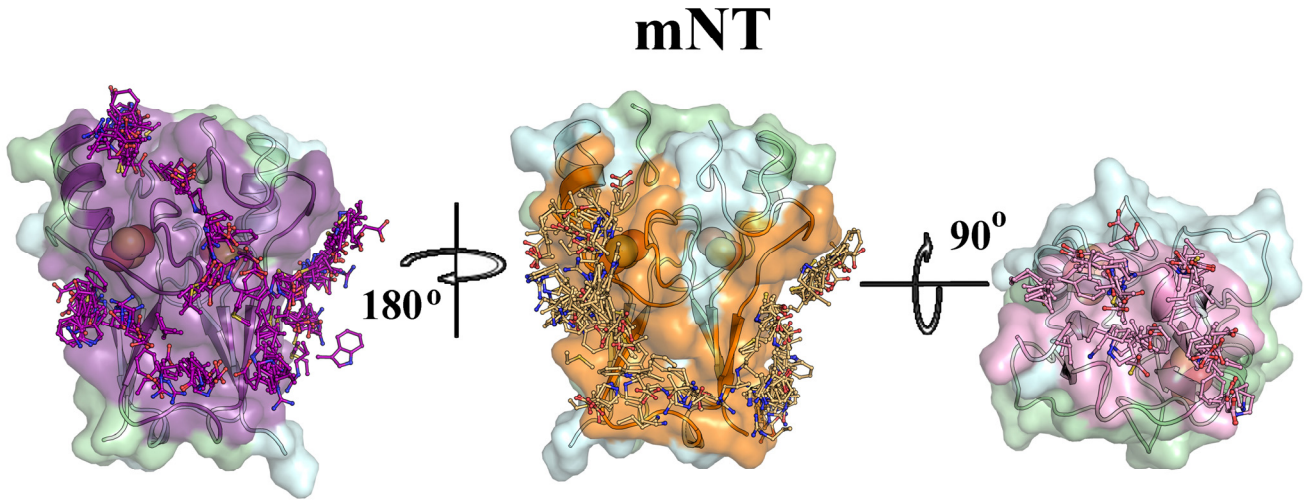

Site 1

Residues: 43, 47-50, 52-55, 57-61, 64-66, 68-71, 75-87, 89-90, 93-94, 100, 102, 104.

Site 2

Residues: 50, 52-55, 57-61, 64-70, 76-79, 82-89, 100, 102,

Site 3

Residues: 62-67, 105-107

B.

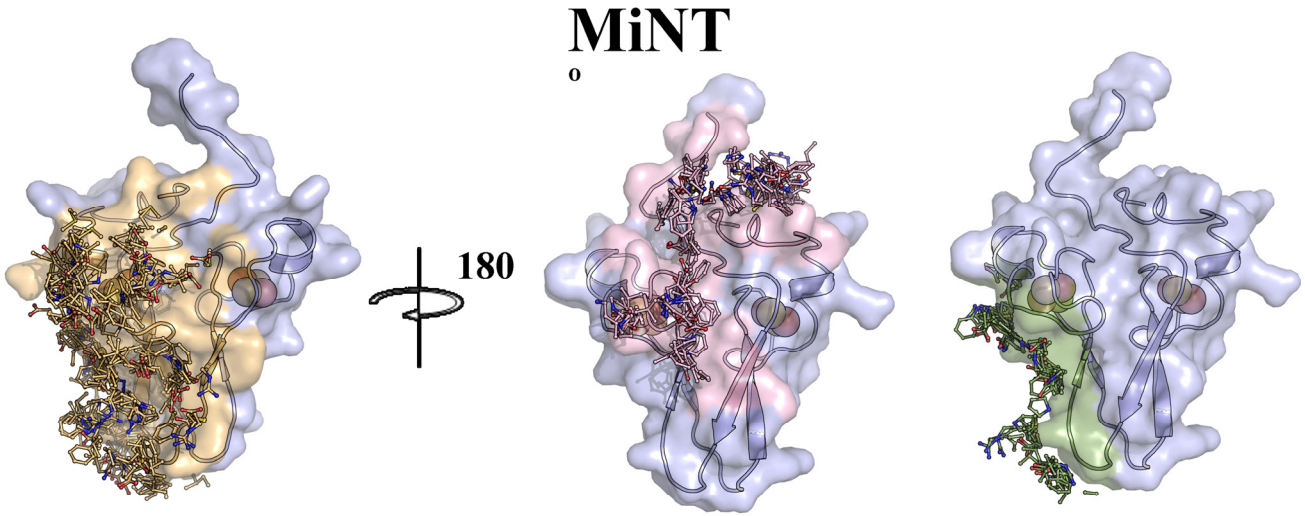

Site 1

Residues: 38, 41, 43, 45-50, 52-53, 59, 61, 82, 85-97, 101-116, 127.

Site 2

Residues: 32-36, 40, 42, 47-49, 63-69, 118-120, 121-122, 124-127.

Site 3

Residues: 52-58, 67, 70-73, 75-76, 81

Figure S4

Dynamic binding mechanism of CISD1 and CISD3 to VDAC

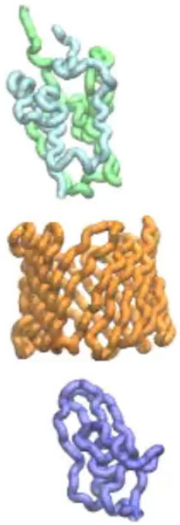

Figure S5 (Movie S1)

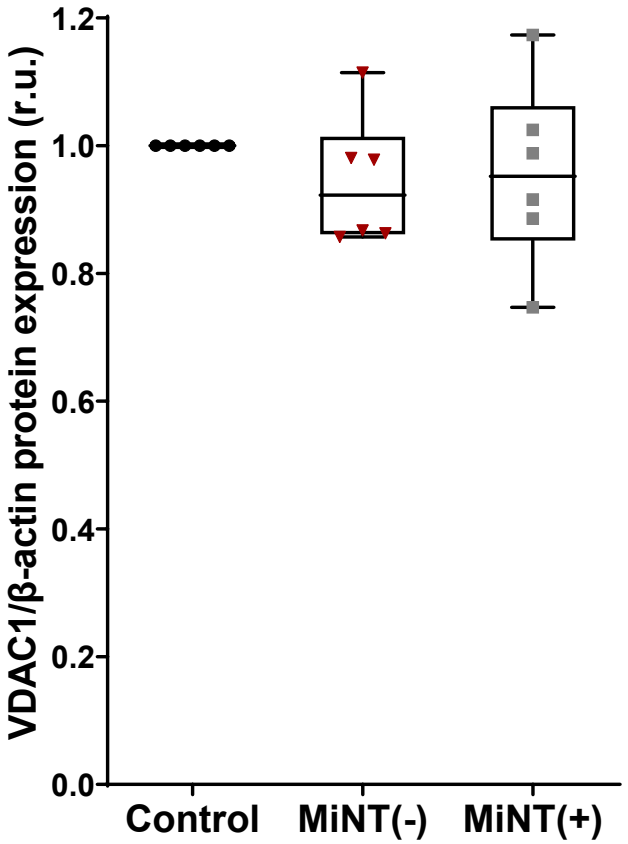
VDAC1/β-actin protein expression (r.u.)
1.2
1.0
0.8
0.6
0.4
0.2
0.0
Control
MiNT(-)
MiNT(+)

Figure S6

Gene names	Accession number	Protein names	MiNT/Blank
ATP5J2	P56134	ATP synthase, H+ transporting, mitochondrial Fo complex subunit F2	10000
NDUFA10	O95299	NADH:ubiquinone oxidoreductase subunit A10	10000
DLD	P09622	dihydrolipoamide dehydrogenase	1000
LACTB	P83111	lactamase beta	1000
MTCH2	Q9Y6C9	mitochondrial carrier 2	1000
PRKCA	P17252	protein kinase C alpha	1000
RPS3	P23396	ribosomal protein S3	1000
SDHA	P31040	succinate dehydrogenase complex flavoprotein subunit A	1000
VDAC1	P21796	voltage dependent anion channel 1	1000
SSBP1	Q04837	single stranded DNA binding protein 1	3.146371816
NDUFV2	P19404	NADH:ubiquinone oxidoreductase core subunit V2	3.094935662
PAM16	Q9Y3D7	presequence translocase associated motor 16 homolog	3.018905729
PTRF	Q6NZI2	polymerase I and transcript release factor	2.461297266
SLC25A11	Q02978	solute carrier family 25 member 11	2.060810811
FKBP4	Q02790	FK506 binding protein 4	1.953026842
MRPL14	Q6P1L8	mitochondrial ribosomal protein L14	1.936251477
GRSF1	Q12849	G-rich RNA sequence binding factor 1	1.925576383
CLIC4	Q9Y696	chloride intracellular channel 4	1.895095288
MRPS12	O15235	mitochondrial ribosomal protein S12(MRPS12)	1.850836541
HADHA	P40939	hydroxyacyl-CoA dehydrogenase/3-ketoacyl-CoA thiolase/enoyl-CoA hydratase (trifunctional protein), alpha subunit	1.827219357
SLC25A13	Q9UJS0	solute carrier family 25 member 13	1.737958765
CHCHD3	Q9NX63	coiled-coil-helix-coiled-coil-helix domain containing 3	1.695034247
MRPL16	Q9NX20	mitochondrial ribosomal protein L16	1.687415406
IMMT	Q16891	inner membrane mitochondrial protein	1.686630369
ABCE1	P61221	ATP binding cassette subfamily E member 1	1.678885804
ATP5A1	P25705	ATP synthase, H+ transporting, mitochondrial F1 complex, alpha subunit 1, cardiac muscle	1.651907196
CYC1	P08574	cytochrome c1	1.622064416
SLC25A22	Q9H936	solute carrier family 25 member 22	1.620810568
TUFM	P49411	Tu translation elongation factor, mitochondrial	1.603916254
CDK1	P06493	cyclin dependent kinase 1	1.596598774
ACSL3	O95573	acyl-CoA synthetase long-chain family member 3	1.578947368
CISD1	Q9NZ45	CDGSH iron sulfur domain 1	1.554111122
ALDH18A1	P54886	aldehyde dehydrogenase 18 family member A1	1.549163396
TIMM13	Q9Y5L4	translocase of inner mitochondrial membrane 13	1.524483808
LRPPRC	P42704	leucine rich pentatricopeptide repeat containing	1.521451691
ATP5O	P48047	ATP synthase, H+ transporting, mitochondrial F1 complex, O subunit	1.520551175
PHB	P35232	prohibitin	1.513462106
SLC25A10	Q9UBX3	solute carrier family 25 member 10	1.496482386
HADHB	P55084	hydroxyacyl-CoA dehydrogenase/3-ketoacyl-CoA thiolase/enoyl-CoA hydratase (trifunctional protein), beta subunit	1.486782847
ATP5C1	P36542	ATP synthase, H+ transporting, mitochondrial F1 complex, gamma polypeptide 1	1.482052435
SLC25A1	Q9UBX3	solute carrier family 25 member 1	1.472775685
SLC25A3	Q00325	solute carrier family 25 member 3	1.455542174
SLC25A6	P12236	solute carrier family 25 member 6	1.455542174
CISD3	P0C7P0	CDGSH iron sulfur domain 3	1.436917952

Table S1